American Mineralogist, Volume 94, pages 53–63, 2009

Experimental fluoridation of nanocrystalline apatite

Jill Dill Pasteris* and David Y. Ding†

Center for Materials Innovation and Department of Earth and Planetary Sciences, Washington University in St. Louis, Campus Box 1169, St. Louis, Missouri 63130-4899, U.S.A.

Abstract

Biological apatite, i.e., the major component of teeth and bones, is a widely available source of nanocrystalline apatite. More information is needed about its chemical reactivity in the environment. In the present study, wafers of cross-sectioned dentin and enamel from a modern horse tooth were soaked in phosphate-buffered solutions with NaF concentrations ranging from 0.01 to 2 molar for periods of up to 14 days at about 19.5 °C. The samples were removed at intervals and analyzed by Raman microprobe spectroscopy. Additional, real-time, in-situ Raman spectroscopic analyses were made on some samples during their fluoridation reaction, using an immersible probe. All spectra were deconvolved and their spectral components analyzed for band position, width, and area. Spectral modeling indicates that fluoridation occurred by a kinetically controlled dissolution-reprecipitation process—bioapatite grains partially dissolved and released Ca and P to the F-bearing solution, which caused essentially end-member fluorapatite to nucleate and precipitate, gradually replacing some of the original bioapatite. The replacement process, i.e., fluoridation of the sample, progresses due to the difference in solubility between bioapatite and (highly insoluble) fluorapatite. The bioapatite in (more soluble) dentin reacted much faster and to a much greater extent than that in (less soluble) enamel. These results have implications for paleoenvironmental reconstruction based on the geochemistry of fossil teeth, heavy-metal remediation in soils and water through addition of phosphate phases, and the recommended methods for dental fluoridation in humans.

Keywords: Fluoridation, medical mineralogy, Raman spectroscopy, apatite, fossilization

Introduction

Biologically precipitated apatite [carbonated form of $Ca_5(PO_4)_3(OH)$], i.e., bioapatite, is of scientific interest for several reasons. It is the dominant phase in our bones and teeth, which historically has been called "dahllite," although the IMA-approved name is carbonate-hydroxylapatite. The chemistry, including the isotopic composition, of bioapatite reflects the climate conditions under which its host animal lived, as well as the animal's sources of water and food. Thus, when fossil bones and teeth are chemically analyzed, their isotopic composition can—in principle—reveal past climate conditions (Cerling and Sharp 1996; Koch 1998; MacFadden 2000; Kohn and Cerling 2002; Hoppe et al. 2004; Kohn and Law 2006; Zanazzi et al. 2007). Bioapatite also possesses the much-touted property of nanocrystallinity, and both bones and teeth are nanocomposites of apatite and organic molecules. It is well recognized that the smallest bioapatite crystallites form in bone and dentin and the largest ones in enamel. Determinations of specific sizes vary, but they typically are reported as about 2 nm thickness and tens of nanometers in the other two directions for dentin and bone crystallites compared to about 20 nm thickness and up to a micrometer length for enamel crystallites (Daculsi et al. 1997; Eppell et al. 2001; Skinner 2005; Glimcher 2006). Bioapatite becomes fluoridated during some well-recognized but incompletely understood processes, such as in the dentists' recommended synthetic fluoridation of our teeth and the natural fossilization of animal bones and teeth.

Both natural and synthetic fluoridation of bioapatite lead to a product that is referred to, in bulk, as fluoridated apatite or carbonate-fluorapatite (IMA-approved term), which historically was known as "francolite." The individual nanocrystals in such materials, however, typically are not analyzed separately to determine their specific chemistry or grain-to-grain homogeneity. Instead, research has focused on fluoride-induced changes in the bulk apatitic material—decrease in the solubility of tooth enamel, i.e., enhanced resistance to the acid attack that leads to tooth decay (LeGeros et al. 1985) and enhanced preservation of fossil bone and tooth material (Hassan et al. 1977; McClellan 1980; Zocco and Schwartz 1994; Michel et al. 1996; Bryant et al. 1996; Sharp et al. 2000; Fabig and Herrmann 2002; Trueman and Tuross 2002; Berna et al. 2004; Nemliher et al. 2004).

The present study involves the controlled synthetic fluoridation of cross-sectioned wafers of modern horse teeth. Because of the structure of a horse's tooth, the wafer cross-sections reveal side-by-side the strongly contrasting types of bioapatite in dentin and enamel. The fluoridation process was monitored in real time by Raman spectroscopy, and the differences in response between dentin and enamel bioapatite were recorded.

Materials and methods

Materials

The materials used in the following experiments come from the molar of an ~3 year old horse. The molar was sawn into wafers 2 to 3 mm thick (Fig. 1) using an Isomet (Buehler Ltd., Lake Bluff, Illinois) saw outfitted with a diamond-edged

* E-mail: pasteris@levee.wustl.edu
† Present address: Washington University School of Medicine, 660 S. Euclid Ave., St. Louis, Missouri 63110, U.S.A.

wafering blade. Without any polishing or further treatment, the wafers of tooth were used in the fluoridation experiments described below. In making Raman spectroscopic analyses, the enamel portions of the samples were clearly identified. No distinction was made between cementum and dentin materials in the horse tooth; both are referred to simply as "dentin." The naturally fluoridated teeth from a modern shark (removed from the purchased, sun-dried jaw of a shark, species unknown, caught off the Philippines) were analyzed for comparison purposes.

Non-biological samples used as chemical end-members for comparison with the above biological materials are a several millimeters long, yellow-green hexagonal prism of fluorapatite from Cerro de Mercado, Durango, Mexico; a synthetic fluorapatite powder (produced by Claude Yoder and Mitchell Sternlieb); and synthetic, white hydroxylapatite powder (Sigma Chemical Co., St. Louis, Missouri). Literature values for the fluoride concentration in Cerro de Mercado fluorapatite range from about 3 to 3.9 wt% (e.g., Streck and Dilles 1998; Pan and Fleet 2002; Harlov and Forster 2003). The synthetic fluorapatite is very close to the ideal end-member composition, which has 3.77 wt% F.

Experimental methods

In the fluoridation experiments on the sawn wafers of modern horse tooth, the standard solution consisted of one buffer salt (Gram-Pac) of potassium phosphate monobasic-sodium phosphate dibasic buffer (Fisher Scientific, Fair Lawn, New Jersey) dissolved in 1 L of distilled water, creating a phosphate-buffered solution at pH 6.88 at 20 °C. Such solutions, typically with the addition of NaCl, are commonly used in medical research to stabilize cells and bone, e.g., to prevent bone from dissolving. To this standard solution, appropriate amounts of NaF were added to produce solutions of the concentrations listed in Table 1. In experiments A through H, the tooth wafer was soaked in 50 mL of the phosphate-buffered NaF solution in a glass beaker. After soaking for the amount of time listed in Table 1, the wafer was removed from the solution, allowed to air-dry, and then analyzed with the Raman microprobe. To avoid fluoride depletion in the solution due to reaction, the soaking solutions were replaced with new ones, as indicated in Table 1. For instance, experiments A, B, and C, which all were carried out at the same NaF concentration, extended over a period of 8.54 days. In experiment I, a much larger beaker was used to accommodate 1 L of solution. In both experiments H and I, the wafer remained continuously submerged for the entire indicated time. All experiments were run at 19.5 ± 0.5 °C.

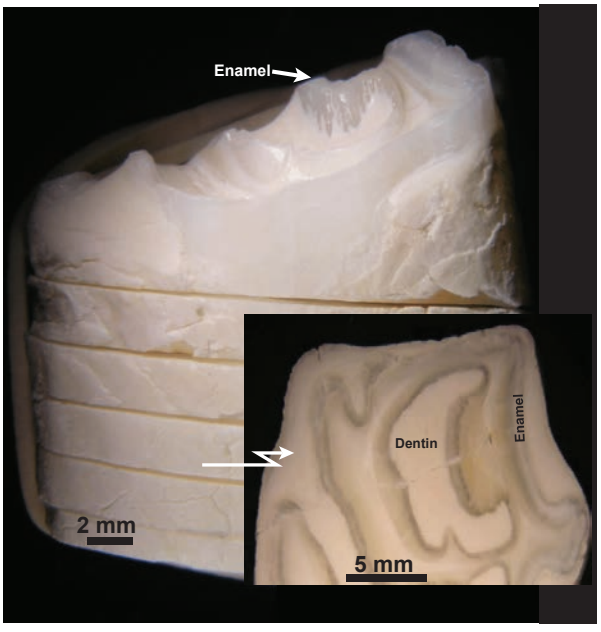

Figure 1. Photograph of the modern horse's molar that was sawed into wafers (see inset) for fluoridation experiments. Inset: In cross-section, enamel forms ribbon-like bands that enclose dentin.

For the real-time, in situ analyses in experiments H and I, each tooth wafer was affixed to the bottom of the beaker with a small piece of synthetic putty, and the solution was carefully poured in. Raman analyses were made using an immersible probe (see below). After some preliminary analyses on several parts of the wafer, spectral acquisition was optimized on a particular spot in the dentin. The instrument was programmed to take spectra automatically on that same spot, beginning with acquisitions every 5 min, changing to every 10 min, and then every 30 min for most of the duration of the experiment. The laser was focused continuously on the spot of interest; only the spectral acquisitions were at timed intervals. At the end of each several-day experiment, analyses were made on several additional areas (mostly in dentin) of the wafer, still using the immersible probe. Comparison of the latter spectra to those taken during the bulk of the experiment permitted assessment of the effect of continuous laser on the primary analysis spot.

Different NaF concentrations were used in several (groups of) experiments, ranging from 1.05×10^{-2} molar NaF (i.e., 4.4 mg NaF/10 mL solution, a standard concentration in fluoridated mouth rinses) to 2 molar NaF. The solutions were not stirred, and all solutions remained clear throughout the experiments. The differences among the solutions provided some opportunity to observe possible effects of NaF-concentration differences on the apatite.

Analytical procedures

Appropriate characterization of such nanocrystalline materials is a challenge. Clearly, standard microbeam techniques analyze large numbers of nanocrystallites simultaneously in each measurement. Moreover, in the case of the nanocomposite dentin, the inseparable organic material is measured simultaneously with the mineral of interest. Most microbeam techniques and all nanobeam techniques also require considerable sample preparation, making it difficult to analyze just the upper few micrometers of a (reacted) nanocrystalline sample. We opted to use Raman spectroscopy on our experimental run products for several reasons, including its ability to make analyses in situ in real time on a sample undergoing a reaction and the ease with

Table 1. Conditions of fluoridation of wafers of horse tooth

Exp.	Experiment duration	Tooth wafer	Concentration of NaF in phosphate-buffered solution	Solution and sample changes	Cumulative time at one concentration	Cumulative time, total per wafer
A	6 h	5	1.05×10^{-2} *M*‡	New solution		6 h
B	7 h	5	1.05×10^{-2} *M*			13 h
C	8 days	5	1.05×10^{-2} *M*		8.54 days @ 1.05×10^{-2} *M*	8.54 days
D	1 days	5	3 wt% H_2O_2		N/A	
E	1.25 days	5	2.10×10^{-2} *M*§	New solution		9.79 days
F	2 days	5	2.10×10^{-2} *M*	New solution		11.79 days
G	2 days	5	2.10×10^{-2} *M*	New solution	5.25 days @ 2.10×10^{-2} *M*	13.79 days
H*	5 days	4a	2 *M*	New wafer and solution	5 days @ 2 *M*	5 days
I†	7 days	4a, 4b	1 *M*	New wafer and solution	7 days @ 1 *M*	4a: 12 days 4b: 7 days

* New tooth wafer, 4a, used here. Automated Raman spectral collection every 30 min. Replaced solution about mid-way through experiment.
† Used 1 L of solution instead of just 50 mL of solution. New wafer, 4b, was analyzed by automated Raman spectral collection every 30 min. Wafer 4a also resided in solution the entire time, but was not analyzed until end of the 7 days.
‡ 4.4 mg/10 mL NaF, i.e., a common concentration in fluoridated mouth rinses.
§ 8.8 mg/10 mL NaF.

which the spectral bands for the mineral phase could be distinguished from those for the organic phase.

Raman analyses were made using a HoloLab Series Laser Raman Microprobe (Kaiser Optical, Ann Arbor, Michigan). The spectrometer-detector system is fiber-optically coupled to the probe head. In our case, two probe-head configurations were used. The dominant configuration makes use of a short-focal-length, immersible optic that consists of an f/2.0 lens integrated into the tip of a metal cylinder 25.4 cm long. This configuration was used for real-time in situ Raman analysis of the horse-tooth wafers submerged in a fluoride solution. The other configuration integrates the probe head into a HoloLab Series 5000 Raman microscope based on a Leica research-grade DML microscope equipped with both transmission and reflection optics. The microscope configuration was used to analyze dry materials. For both the immersible-probe and microprobe configurations, irradiation is by a 100 mW, 532 nm, frequency-doubled Nd-YAG visible laser, delivering a maximum of 11 mW to the sample surface in the microprobe configuration. The spectral range reported is 100 to 4000 Δcm^{-1} at a resolution on the order of 3 cm^{-1}, acquired with an f/1.8 Holographic Imaging Spectrograph. The full range is captured in a single acquisition, using an Andor high-resolution, thermoelectrically cooled CCD array detector with 2048 channels. Typically, 32 acquisitions of 4 s each were taken and then averaged into a single spectral analysis.

Both analytical configurations were calibrated for wavelength and intensity using a He-Ne gas excitation lamp and a NIST-referenced intensity lamp, respectively. The calibration algorithms are automatically applied to the raw data using Kaiser's "HOLOGRAM" software. Thus, the output spectra (see "Data handling" section below) are already corrected for intensity and Raman peak position. Positions are given here to the nearest 0.1 Δcm^{-1}. Reported positions are accurate to within ± 0.3 Δcm^{-1}, and reproducibility is ± 0.1 Δcm^{-1} based on repeated analysis of the same silicon wafer and hydroxylapatite standard during each measurement session.

The two analytical configurations offer different analysis capabilities. With the microscope, one can visualize and photograph specific areas of the sample and see exactly where the laser beam is focused. Using the microscope and an 80× ultra-long-working-distance objective with a numerical aperture of 0.75, the spatial resolution of the individual analyses is on the order of a couple of micrometers. The effective penetration depth of the laser into these nanocrystalline samples is probably less than 2 μm. In contrast, the immersible probe tip has a spatial resolution of about 15 μm on a solid sample in a solution (only a few micrometers penetration depth), and this configuration lacks the sight-through-the-optics capability of the microscope.

For the in-situ, real-time fluoridation analyses, ~20 mW of focused laser power was delivered to the sample surface by the immersion probe, as measured in air. The focused beam was visually aligned (sighting through the glass vessel and transparent solution) on the desired portion of the tooth, i.e., dentin or enamel. The vertical (via a sensitive lab jack) and horizontal (via an x-y drive) alignments of the sample were optimized while trial spectra were acquired. Two modes of spectral collection were used: (1) the operator moved the sample between analyses, permitting evaluation of the homogeneity of reaction throughout the sample and the comparison of reaction in dentin with that in enamel, and (2) the operator optimized the focus on a single point in the dentin or enamel and set the Raman system to automatically acquire one spectrum every 30 min over a period as long as several days. In the latter case, the signal strength of the spectrum, as an indicator of proper focus, was checked at intervals to assure high signal:noise ratios. This routine permitted evaluation of the progress of the fluoridation reaction.

Electron microprobe analyses were performed on one shark tooth to aid the "calibration" of Raman peak position with respect to the fluoride concentration of bioapatite. The electron microprobe is a JEOL JXA 8200 Superprobe with five wavelength-dispersive spectrometers and a silicon-drift energy dispersive spectrometer (EDS). Analyses were made at 15 kV accelerating voltage and 25 nA current, using a beam diameter of 20 μm. A synthetic fluorphlogopite with 9 wt% F was used as the fluoride standard, and fluoride intensities were projected back to t_0 to correct for time-dependent variation in the measurement of F$K\alpha$ intensity. Based on published bulk compositions of enamel (Skinner 2005), the shark enameloid was assumed to contain 8 wt% H_2O and 2 wt% CO_2. Using EDS, no Cl could be detected, but F was readily detected in the enameloid. Analysis totals were 100 ± 3 wt% except where indicated.

Data handling

Individual Raman peaks were deconvolved, i.e., resolved into the sum of multiple bands, using the spectral software GRAMS 32 AI, version 6.00 (Galactic Industries Corporation, Salem, New Hampshire). There are several user-controlled parameters in the deconvolution program: (1) the spectral bands were declared to be a mixture of Gaussian and Lorentzian in shape; (2) deconvolution was done on the spectral interval 700–1200 Δcm^{-1}, typically without background correction; (3) the number of deconvolved bands typically was set at 6 to 10, depending upon whether collagen was present in the sample (abundant in dentin, but absent in enamel); and (4) the most prominent apatite peak at about 960 Δcm^{-1} was deconvolved into two bands, i.e., the dominant ν_1 P-O symmetric stretch at 960–964 Δcm^{-1} and a smaller band centered about 10–15 cm^{-1} lower.

Based on the operator-directed deconvolution of a spectrum, the GRAMS 32 software calculates for each derived band its center at half-maximum intensity, area, maximum intensity, full width at half maximum, and the proportion of Gaussian and Lorentzian character. The calculated band positions, widths, and areas are used in the present discussion. Band areas and ratios of them are particularly sensitive to the selection of where the bands are centered and how many bands there are. The presence of collagen in the modern dentin samples was accounted for in the determination of the areas of the mineral bands. The deconvolution procedure followed protocols developed in our laboratory, based on the Raman analysis of bones and teeth from numerous types of mammals, birds, and fish.

A calculated mixing model also was evaluated through spectral simulation. For this model, a representative spectrum of initially low-fluoride horse dentin was added together in different proportions with the spectrum of the high-fluoride geological apatite from Cerro de Mercado, Mexico. The modeling simulated the dissolution of bioapatite and its replacement by end-member

fluorapatite (FAp). The spectral additions are of the following type: (1000 × dentin spectrum); (999 × dentin spectrum) + (1 × FAp spectrum); ... (700 × dentin spectrum) + (300 × FAp spectrum). Approximately 80 synthetically produced spectra were generated in the above series. For purposes of deconvolution and evaluation, the resultant spectral sums were treated the same way as the real spectra of actual samples. Because the spectrum of single-crystal natural fluorapatite is much stronger than that of nanocrystalline dentin, these spectral sums do not indicate the exact amount of fluoridation that should occur to reach certain spectral values, but rather indicate only trends in spectral parameters.

Significance of Raman spectral parameters

Raman spectroscopy provides a different kind of sample characterization than more traditional microbeam analyses, such as electron microprobe analysis. Raman spectra do not directly provide the chemical composition of a sample. Rather, they reveal the presence of chemical-structural groups, for instance, the peak representing the ν_1 P-O symmetric stretch within the phosphate tetrahedron in apatite (Fig. 2). In addition, Raman spectroscopy distinguishes the presence of individual phases, analogous to X-ray diffraction (XRD), rather than providing an aggregated chemical analysis of all phases in the irradiation volume, as does electron microprobe analysis. Important aspects of a phase's chemistry can be revealed, however, by a Raman spectrum. For instance, the spectrum of the calcium-phosphate mineral apatite is different not only from spectra of other metal phosphate phases, but also from those of all the other calcium phosphate phases. Thus, Raman spectra provide important, semi-quantitative compositional information, somewhat analogous to the compositional information that can be inferred from XRD patterns.

Raman spectra reveal significant differences between the bioapatite in enamel and dentin, as well as document specific types of changes in those materials. For instance, the spectra (Fig. 2) show abundant hydroxyl (OH^-) in the enamel apatite but only very low concentrations (near the detection limit) of OH in apatite in the dentin (see Pasteris et al. 2004 and references therein). Whereas the ~1073 Δcm^{-1} band, indicating carbonate substitution (Penel et al. 1998; Awonusi et al. 2007; Tacker 2008) in the apatite, is rather subdued in spectra of enamel, it is strongly visible in dentin, which typically contains about 6–7 wt% carbonate compared to about 3.5 wt% in enamel (LeGeros 1981; Daculsi et al. 1997; Elliott 2002). In samples of dentin, the spectra also reveal multiple peaks for C-C, C-H, and N-H vibrations that indicate the presence of collagen, the fibrous protein that forms a nanocomposite with the nanometer-scale crystallites of bioapatite. Ratios of the measured areas of the deconvolved spectral bands associated with different vibrational modes can be used to infer differences between or changes in the molar proportions of identifiable components, e.g., mineral (apatite) and collagen (Penel et al. 1998; Timlin et al. 1999; Carden and Morris 2000; Pasteris et al. 2004; Awonusi et al. 2007).

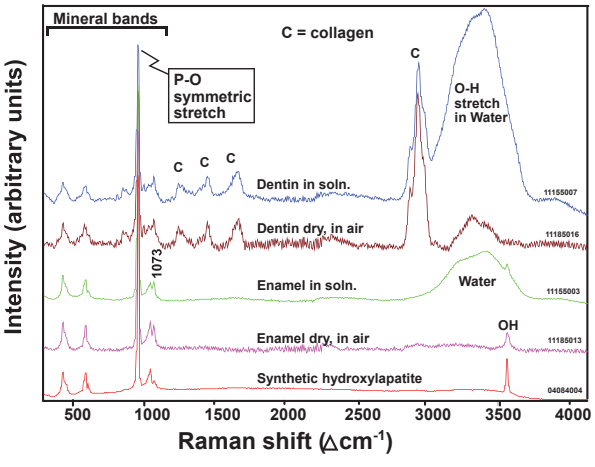

Figure 2. Raman spectra of dentin and enamel from a horse-tooth wafer and of synthetic hydroxylapatite powder (Sigma Chemical Co., St. Louis, Missouri). Spectral bands for collagen (labeled "C") appear only in spectra of dentin. "In air" spectra recorded on dry samples using the microscope configuration; "in solution" spectra recorded with the immersible probe while the samples were submerged.

The positions of the individual peaks detected in a given material can be assigned to specific vibrational modes within its structure. Minor shifts in the positions of these peaks typically indicate chemical substitution within the material. Our analyses of synthetic standards show that the position of the P-O symmetric stretch moves from about 961.6 Δcm^{-1} in pure hydroxylapatite to about 964.6 Δcm^{-1} in end-member fluorapatite. The specific position or change in position of this Raman band therefore can be used as a semiquantitative indicator of fluoride concentration in the apatite sample, as is done in the current study (see Fig. 3). Carbonated apatites, both synthetic and natural biological ones, can have P-O band positions below 960.5 Δcm^{-1} (Pasteris et al. 2007).

The widths of the Raman spectral peaks of a solid indicate the relative degree of atomic ordering within its lattice. High-temperature geological apatite with a high degree of crystallinity, for instance, has narrower Raman peaks than low-temperature synthetic precipitates of the same composition (see Pasteris et al. 2004; Wopenka and Pasteris 2005). Nanocrystalline bioapatite, especially in dentin and bone, has a much lower degree of atomic order and thus much wider peaks than do macrocrystalline, geological apatite samples. So it is that enamel, with its much larger crystallite size than dentin, has narrower Raman peaks than the latter (Fig. 2). Because the fluoride ion fits more symmetrically into the apatite structure than does the OH^- ion (Hughes and Rakovan 2002), the Raman peaks of fluorapatite are inherently narrower than those for hydroxylapatite formed under comparable conditions.

Results

Results of the fluoridation experiments

The incorporation of fluoride into bioapatite can occur either in the primary biological growth process, as in the teeth of numerous fish, or in a secondary replacement process, e.g., synthetic fluoridation in the dentist's chair or geochemistry laboratory (current case) and natural geological fluoridation of fossil bones and teeth. The present Raman analyses of synthetically fluoridated bioapatite can be placed into context by reference to spectra of a typical, gradationally fluoridated, modern shark tooth. The latter provides a large range in its spectral properties

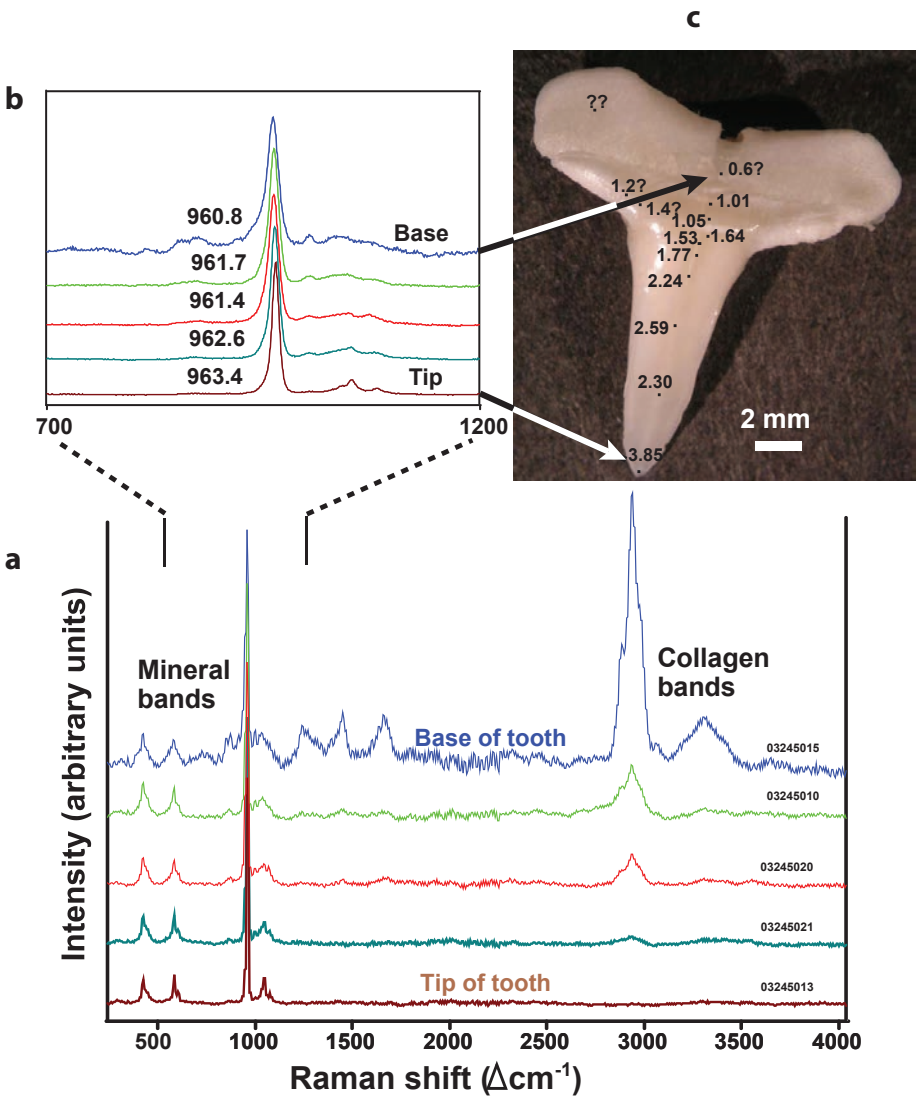

FIGURE 3. Base-to-tip Raman spectroscopic traverse of a modern shark's tooth. Individual spectra taken with microscope configuration, focused on outer enameloid surface of tooth. (**a**) Progression from dentin-like base to tip shows decrease in collagen concentration, as collagen bands weaken and then disappear. (**b**) Enlargement of one spectral region shows increase in fluoride concentration (upward shift in band position of P-O stretch) and narrowing of peak. (**c**) Numbers indicate wt% F concentration at marked spots, as determined by electron microprobe analysis. Question marks indicate analyses whose totals are (much) less than 97 wt% due to high content of organics. Raman analyses not taken at exact same spots.

and acts as a natural, biological model of fluoridation. Two teeth, removed from the shark's cartilaginous jaw, were analyzed on their exterior surfaces from the base to the tip of the tooth. The spectral differences as a function of position along the tooth are quite systematic (Fig. 3). In traverses from the base to the tip of the tooth, the position of the nominal 960 Δcm^{-1} band (P-O symmetric stretch) shifted nonlinearly to higher values, whereas the ratio of the area of each major collagen band to the area of the mineral's P-O stretch band decreased very rapidly as the traverse passed from the base to the projecting shaft of the tooth (Fig. 3a). No collagen bands were detected at or near the tip of the tooth. As the wavenumber position of the P-O stretch increased, reflecting an increase in concentration of fluoride, the peak became narrower, indicating an increase in the degree of atomic order of the mineral (Fig. 3b).

Electron microprobe analysis of the surface of a third shark tooth confirmed that the tip is essentially end-member fluorapatite (3.85 wt% F) and that the fluoride concentration of the apatite decreases toward the dentin-like base of the tooth (Fig. 3c). The fluoride concentration gradient is irregular, making it difficult to associate a Raman analysis (i.e., band position) with the appropriate fluoride concentration. Thus, accurate calibration of specific Raman band position with respect to fluoride concentration remains to be done.

The spectral parameters of position and width for the peak centered at about 960 Δcm^{-1} proved important not only in the spectra of the shark teeth, but also in the synthetically fluoridated horse tooth. An x-y plot of these two parameters in Figure 4 demonstrates the parallelism but non-overlap of the trends for the modern shark teeth and the synthetically fluoridated dentin. The negative slopes of these trends confirm the correlation between peak narrowing and shift in position, both in response to an increase in fluoride concentration. Figure 4 also shows one important spectral difference between dentin and enamel in the horse tooth, namely that the unreacted enamel's bioapatite is much more atomically ordered than the dentin's bioapatite. Thus, the Raman band width for enamel is distinctly narrower than that for dentin. The exterior surface of the shark tooth, i.e.,

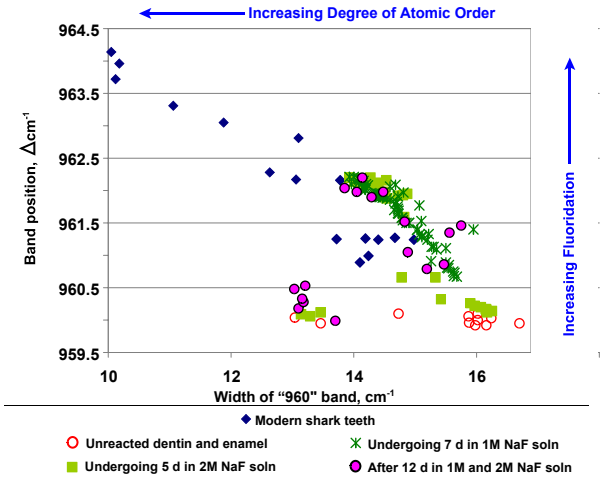

FIGURE 4. Position (mid-point at half-maximum intensity) and width (full width at half-maximum intensity) of the deconvolved band representing the P-O symmetric stretch in apatite. Natural primary gradation in fluoride concentration of the enameloid of a modern shark tooth compared to the ongoing secondary fluoridation of enamel (narrow band widths) and dentin (wider band widths, initially) of a modern horse tooth. For both shark enameloid and horse dentin, as the apatite becomes more fluoridated (reflected in upward shift in band position), the band width decreases. Size of symbols approximates uncertainty.

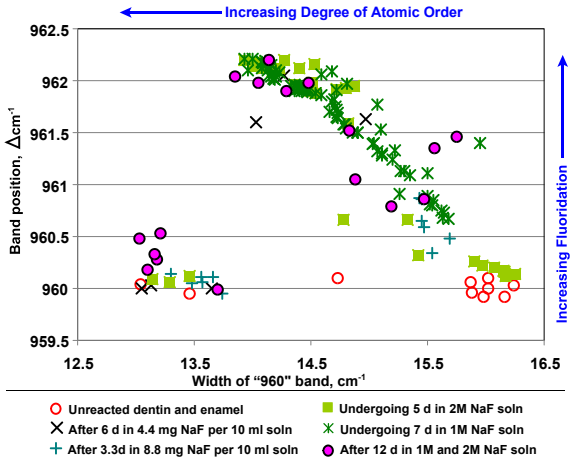

FIGURE 5. Position and width of the P-O stretch in enamel and dentin of horse tooth undergoing synthetic fluoridation. Experiments carried out in solutions of different NaF concentration and with different immersion times. The "undergoing 7d" data represent the longest continuous time over which one point in the dentin was monitored. The composition of the dentin changed much more than that of the enamel for the same experimental conditions. See Table 2 for results of additional experiments.

the material that was analyzed, is actually enameloid rather than enamel; most literature distinguishes these two materials, however, only the basis of the difference between the types of cells that give rise to the mineralization.

Figure 5 displays the 960 band position vs. width data for several of the experiments, carried out at four different concentrations of NaF for lengths of time up to 12 days for one wafer and nearly 14 days for another wafer (Table 1). In addition to representing the material characteristics of the analyzed tooth samples, these spectral parameters also record the progress of fluoridation of enamel and dentin. By the end of each experiment, the respective tooth sample showed spectral evidence of some degree of fluoridation, through band shift and narrowing.

To a first approximation, the data for all the fluoridation experiments (not all shown) lie along the same trend in band position vs. width, with only a small number of data points as clear outliers. The dentin component of each wafer consistently showed more spectral change over time during the experiment than did the enamel. In some experiments, only the dentin showed convincing evidence of fluoridation. The experimental data and statistics shown in Table 2 (for experiments C through G and I) represent analyses that were made after the tooth wafer had undergone aqueous reaction for the specified time. In such cases, multiple locations in both enamel and dentin were analyzed, and there was no particular spatial relationship between one analyzed point and the next. Such random micro-surveys of the exposed surface of the sample indicate that, even after 12 days of soaking in 1–2 *M* NaF solution, the degree of fluoridation of the bioapatite is very heterogeneous (see also in Fig. 5). Moreover, this end-stage analysis recorded not only some of the most fluoridated dentin and enamel regions, but also some of the least fluoridated. The analyses in Table 2 indicate that the band positions of the bioapatite (especially dentin) gradually shifted upward and showed

TABLE 2. Spectral data acquired before and after fluoridation experiments

Experiment (no. of analyses)	mean ν_1 position, $\Delta cm^{-1} \pm 1$ std	mean ν_1 width, $cm^{-1} \pm 1$ std
Unreacted dentin (9)	960.0 ± 0.1	16.1 ± 0.3
Unreacted enamel (8)	960.1 ± 0.1	13.3 ± 0.2
Experiment C, after 8 days in 4.4 mg NaF/10 mL solution		
Dentin (3)	960.4 ± 0.4	15.7 ± 0.7
Enamel (6)	960.0 ± 0.04	13.4 ± 0.1
Experiment D, after 8.5 days in 4.4 mg NaF/10 mL solution		
Dentin (1)	960.9	15.5
Enamel (5)	960.0 ± 0.1	13.6 ± 0.2
Experiment E, after 1.3 days in 8.8 mg NaF/10 mL solution		
Dentin (1)	960.6	15.6
Enamel (6)	960.1 ± 0.05	13.7 ± 0.2
Experiment F, after 2 days in 8.8 mg NaF/10 mL solution		
Dentin (6)	960.6 ± 0.2	15.5 ± 0.1
Enamel (6)	960.1 ± 0.1	13.6 ± 0.2
Experiment G, after 8.3 days in 8.8 mg NaF/10 mL solution		
Dentin (6)	961.0 ± 0.5	15.5 ± 0.7
Enamel (3)	960.3 ± 0.1	13.8 ± 0.1
After Experiment I: 5 days in 2 *M* and 7 days in 1 *M* NaF		
Dentin (11)	961.6 ± 0.5	14.8 ± 0.7
Enamel (6)	960.3 ± 0.2	13.2 ± 0.2

Note: Raman microprobe analyses made on dry wafers after each experiment was completed.

larger standard deviations as fluoridation progressed.

A different analytical approach was used in the back-to-back experiments on tooth wafer 4a, which initially was soaked for 5 days in 2 *M* NaF and then 7 days in 1 *M* NaF (experiments H and I, respectively). Analyses were made in situ by means of the immersible probe. During the initial 5-day experiment, three different spots on wafer 4a were analyzed sequentially, each for tens of hours. One reason for moving the Raman immersion probe to a new location after monitoring a specific site for many hours in solution was to determine if the irradiation of a given point by the laser beam had enhanced or hindered fluoridation of the apatite (cf. Nammour et al. 2005). Our statistically small sampling gave no evidence of laser-induced differences in the apatite's response to fluoridation, i.e., in some cases the newly irradiated spot showed more fluoridation than the long-irradiated spot, and in some cases, the reverse. We believe our 5-day data represent the chemical-structural change over time of three unrelated micro-aliquots of nanocrystalline bioapatite.

The subsequent 7-day experiment was carried out on a different wafer (4b), in a 1 *M* solution of NaF. The laser was focused on the same point in wafer 4b during the entire time, and spectra were recorded once every 30 min. This large data set (Fig. 5, asterisks) therefore records the spectral changes in a single volume of dentin as it underwent fluoridation. The band position vs. width relation is very narrowly defined and consistent with the trend delineated by spectra from analyses of random points in other experiments. The 7-day data define a fairly linear pattern, but there is a distinct inflection toward smaller band widths at about 962 Δcm^{-1}. Wafer 4a also was immersed the entire 7 days (unmonitored) in this 1 *M* solution after having been immersed 5 days in the 2 *M* NaF solution; it was analyzed after completion of the second experiment (see Table 2). Note that, even after undergoing both experiments, some parts of the dentin still had incorporated little fluoride (see Fig. 5, dark-shaded circles). The highest-fluoride analyses (i.e., highest band positions) after 12 days of soaking showed no greater fluoride concentration than some of those taken on samples after 5 days. Use of 2 *M* NaF had no greater effect on band position than did 1 *M* (lightly shaded squares cf. asterisks). One analysis taken after 6 days of soaking in only 1.05×10^{-2} *M* NaF solution (Fig. 5, black "X") showed almost as high a band position as the analyses of samples in the 1 and 2 *M* solutions.

Results of spectral modeling

The chemical-structural nature of the synthetically fluoridated samples can be considered in light of two end-member materials models (see Fig. 6), i.e.: (1) the sampled volumes are homogeneous among their grains, all of which express a specific solid-solution composition that is enriched in fluoride compared to a postulated low-F bioapatite, e.g., 1000 grains, each of which is $OHAp_{90}FAp_{10}$ (Model 1), where OHAp = pure hydroxylapatite and FAp = pure fluorapatite; or (2) the sampled volumes are physical mixtures of low-F (unreacted) bioapatite plus different amounts of nearly end-member FAp, e.g., 900 grains of $OHAp_{100}$ + 100 grains of FAp_{100} (Model 2). Note that purely chemical analysis, as by electron microprobe, cannot distinguish between these two models given the nanometer-scale of the bioapatite grains.

Our experimental data (Figs. 4 and 5) clearly show that, in the fluoridation of bioapatite, the 960 Δcm^{-1} component of the main peak: (1) shifts upward in position, and (2) becomes more narrow. Generally speaking, these same two effects are expected whether one analyzes homogeneous apatite grains that develop different OHAp-FAp solid-solution compositions (Fig. 7, panel I) or aggregates of grains of two end-member compositions (Fig. 7, panel V). Distinguishing between these two possibilities requires closer examination of spectral trends.

Figure 8b is an enlargement of part of Figure 5, showing the specific relation between band position and width of the nominal 960 Δcm^{-1} band in the measurements made on the exact same spot in dentin during 7 days of fluoridation (experiment I). This enlarged view of the decrease in band width as band position

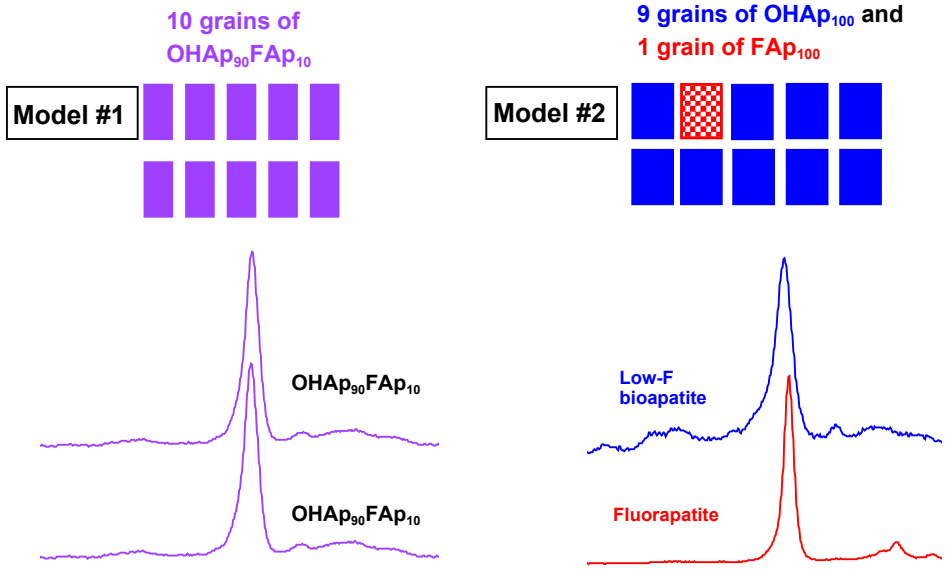

FIGURE 6. Two models of the nature of fluoridated tooth apatite: (1) Individual grains of initially low-F bioapatite have become homogeneous grains of OHAp-FAp solid solution, and (2) initially low-F bioapatite has become a mixture of original grains and essentially end-member FAp. These materials models can be coupled with models of the mechanism of grain formation (see Fig. 7).

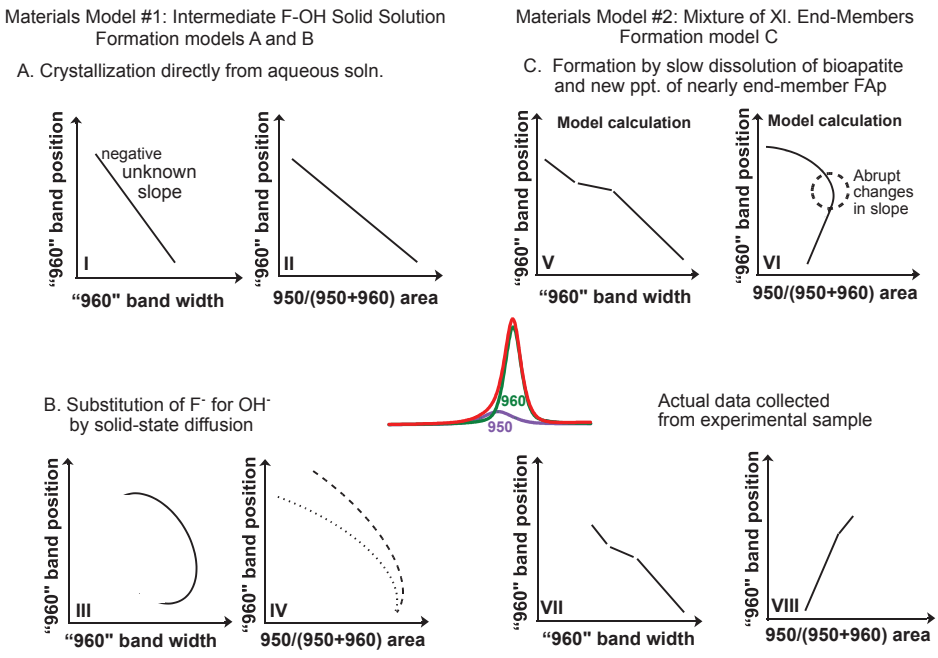

FIGURE 7. Illustration of spectral properties expected via two different models (1 and 2) of the material nature of experimental run products and the fluoridation mechanisms (A, B, and C) that could give rise to such products. Panels I and II: Smooth transition in spectral properties expected among members of continuous solid solution series. Panels III and IV: Random replacement of OH^- ions by F^- ions expected to cause increasing atomic disorder in structure until fluoride is dominant. Panels V and VI: Due to strong difference in shape and peak position between low-F bioapatite and FAp, spectral trends are expected to show discontinuities as fluoride begins to dominate. Panels VII and VIII: Schematic representation of spectral results from experimental run products (real data points shown in Fig. 8).

shifts upward reveals distinct semi-parallel diagonal trends connected by horizontal offsets. The same stairstep-like pattern is demonstrated by the mixing-model spectra (see Fig. 8a), which are weighted sums of the spectrum of geological fluorapatite and the spectrum of an untreated sample of horse dentin, as described in the "Data handling" section. The data points derived from this mixing model show a prominent inflection toward lower band widths at about 963.3 Δcm^{-1}, i.e., about 1 wavenumber higher than where the data from the 7-day fluoridation experiment show a similar inflection. Note that the ranges of the vertical (and horizontal) axes in Figures 8a and 8b are different, but that the presence of breaks in slope is similar in both.

Analysis of how the shape of the actual spectral trace changes during fluoridation is another means to distinguish between the two materials models, i.e., homogeneous solid solution vs. mixture of end-members. An important aspect of peak asymmetry is represented by the area of the 950 Δcm^{-1} deconvolved band component divided by the sum of the areas of the 950 and 960 Δcm^{-1} bands (see Fig. 7, center insert and panels II and VI). In the characterization of progressively more FAp-rich members of an apatite solid-solution series (i.e., material model 1), one would expect a relatively symmetric narrowing of the spectral trace. Such narrowing would decrease the area of the 950 Δcm^{-1} deconvolved band component of the spectrum, ultimately eliminating it (see Fig. 7, panel II), as observed in the geologic fluorapatite used in this study. If the experimental products, however, were a mixture of end-member FAp and low-F bioapatite (i.e., materials model 2), one would expect evidence of increasing asymmetry in the spectral trace due to the strong difference in both shape and position between the bioapatite and fluorapatite traces (Fig. 6, bottom right). As bulk fluoridation increased, the area of the 950 Δcm^{-1} deconvolved band component would become an increasingly larger proportion of the sum of the areas of the 950 and 960 Δcm^{-1} bands (see Fig. 7, VI). The evaluation of asymmetry presented in Figures 8c and 8d shows a tight fit of the 7-day experimental data set to two lines of different, but positive, slopes that intersect at about 962 Δcm^{-1}, i.e., the inflection point noted earlier (Fig. 8d). The synthetic spectra from the spectral mixing model also show an initially linear increase in peak asymmetry with fluoride concentration and then a change in slope (see Fig. 8c). The model calculations actually show the correlation curve looping back (Fig. 7, panel VI) as the degree of fluoridation increases beyond that of the experimental samples.

DISCUSSION

The mechanism of fluoridation of nanocrystalline apatite would be much simpler to understand if we could monitor the properties of individual nanometer-scale grains. Instead, we face the dual challenges of (1) interpreting the analyses of material *properties* to understand a *process*, i.e., fluoride incorporation, and (2) analyzing *micro*-scale volumes of bioapatite to infer how fluoridation occurs at the *nano*-scale of the mineral grain.

Plausible models of fluoridation

The two materials models (Fig. 6) also suggest specific chemical mechanisms by which fluoridation of bioapatite could take place (Fig. 7, lettered formation models). Materials model 1, for instance, represents the situation expected if a diffusional front moves through the dentin, causing solid-state replacement of many of the OH^- ions in apatite by F^- ions (formation model B). One could postulate the development of equilibrium between the fluoride concentration of the altered apatite and that in the solution, given sufficient time. Materials model 2, in contrast, represents the situation expected if some grains of low-fluoride bioapatite dissolve and are replaced by end-member fluorapatite. The data shown in Figure 8a for the spectral mixing model

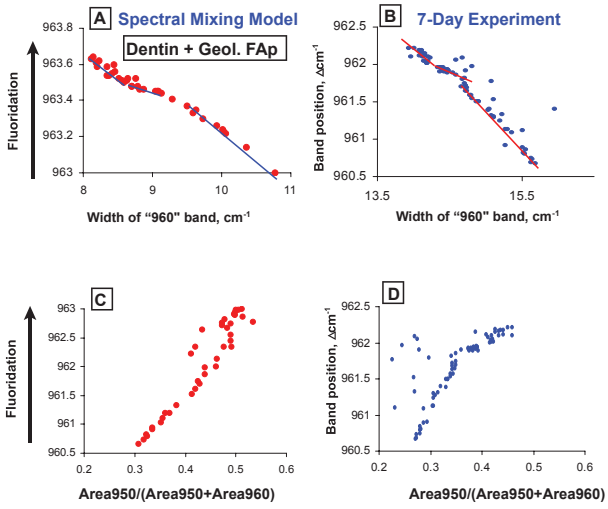

FIGURE 8. Comparison of parameters from actual spectra taken during the 7-day fluoridation experiment (right side) with those generated by modeling (left side) the weighted sums of an actual dentin spectrum and a spectrum of geological fluorapatite, e.g., (900 × dentine spectrum) + (100 × FAp spectrum), (890 × dentine spectrum) + (110 × FAp spectrum), (700 × dentine spectrum) + (300 × FAp spectrum). (**a** and **b**) Line segments added to show the trends in band width as fluoridation progressed and to highlight the step-like discontinuities for both the experimental run products (**b**) and modeled spectral sums (**a**, **c**, and **d**) Spectral expression of the shape (essentially degree of asymmetry) of the nominal 960 Δcm^{-1} peak as fluoridation progressed in both the experimental run products (**d**) and modeled spectral sums (**c**).

actually were calculated by assuming a fixed number of dentin grains (each with the same end-member dentin spectrum) that incrementally were removed (i.e., their spectra subtracted) and replaced with Cerro de Mercado fluorapatite (i.e., add one FAp spectrum for each bioapatite spectrum removed). The reason for using a geological FAp as an end-member rather than a bioapatite FAp from the tip of the shark tooth is the uncertainty about the nanocrystalline bioapatite; the geological FAp is coarsely crystalline and structurally well understood.

Fluoridation model based on the samples analyzed

Our experiments were carried out in phosphate-buffered solutions to prevent extensive dissolution of bioapatite in the wafers of horse tooth. However, the solid samples did change significantly in composition over a period of days. Figure 7 illustrates how the difference in band shapes between fluorapatite and bioapatite can be exploited to infer the specific mechanism of fluoridation. Panels I–VI of Figure 7 are sketches of spectral changes predicted to occur due to different mechanisms of fluoride incorporation; for comparison, panels VII and VIII are sketches of actual data trends in the 7-day continuous monitoring of one small volume of dentin. Those data trends rule out both of the formation models (A and B) for creation of a homogeneous solid solution.

The response of the actual spectra to attempts to deconvolve them, especially at high degrees of fluoridation, highlights the need to understand how abrupt changes can occur in spectral parameters. The asymmetric ~960 Δcm^{-1} bioapatite peak is readily deconvolved into 950 and 960 Δcm^{-1} components (see inset in middle of Fig. 7) of reasonable shape for Raman bands. Spectral addition (according to formation model C) of the narrow 964 Δcm^{-1} peak of geological FAp to dentin's asymmetric 960 Δcm^{-1} peak, however, generates a peak shape that is both asymmetric and skewed to higher wavenumbers than in typical bioapatite. One might envision the 960 Δcm^{-1} peak as becoming "smeared." As the ratio of the number of FAp spectra to the number of dentin spectra increases in the modeling exercise, these synthetic spectra, like the actual spectra collected in the 7-day experiment, become increasingly difficult to deconvolve by standard methods. In both the modeled and actual spectra at high degrees of fluoridation, the peak shape is not what is expected of the Raman spectrum of a single, homogeneous phase. This deviation from expected Raman band shape leads to changes in slope in the data trends of both the actual spectra and those generated with the mixing model (Fig. 7, panels VII and VIII cf. V and VI; Figs. 8a, 8c, cf. 8b, 8d). Such spectral addition is what would occur if original bioapatite grains were dissolved and replaced by end-member FAp, i.e., formation model C.

Spectral band-shape analysis does not support the alternative model of formation (cf. materials model 1) that involves the progressive, homogeneous transformation of the original bioapatite into increasingly more fluoride-rich samples of OHAp-FAp solid solutions. Other aspects of the dentin's response also refute the solid-solution model, whose mechanism seems limited to diffusive exchange of OH^- for F^- in the solid bioapatite (over a period of days at room temperature) or wholesale dissolution of bioapatite and subsequent reprecipitation of an equilibrium composition of OHAp-FAp. Solid-state diffusive replacement of OH^- by F^- in the bioapatite at room temperature would not be expected (in the absence of secondary recrystallization) to markedly improve the atomic ordering in the apatite (see Fig. 7, panel III). Thus, solid-state diffusion does not explain the significant peak-narrowing demonstrated in our experiments. Likewise, broad-scale dissolution and reprecipitation of equilibrium, fluoride-enriched apatite is inconsistent with the patchiness in composition that was documented by our spatially distributed point analyses. In addition, volumetrically significant dissolution-precipitation (Fig. 7, model A) should have produced measurably different compositions of apatite between the experiments done at the highest and lowest concentrations of NaF. Instead, the apatite compositions are very similar among all the experiments.

Our proposed model of incremental replacement of dentin by end-member FAp is based on the availability of an excess of fluoride from the experimental solution and phosphate from the buffer. It appears that calcium was the controlling component in the process, in that calcium could have come only from dissolution of bioapatite. The key to our proposed replacement mechanism of fluoridation is the significantly lower solubility of FAp than bioapatite, i.e., carbonated OHAp. Many conflicting solubility products have been published for FAp and OHAp, but all the data agree that FAp's solubility product is one to several orders of magnitude less than that of OHAp (Elliott 2002; Rakovan 2002). Because the solubility of (carbonated) bioapatite is significantly greater than that of OHAp (LeGeros 1981; LeGeros and LeGeros 1984; Baig et al. 1999; Mann 2001; Gross and Berndt 2002; El-

liott 2002; Barry et al. 2003), the dissolution of bioapatite would release concentrations of aqueous calcium and phosphate greatly in excess of those required for saturation with respect to FAp—once fluoride was introduced into the solution. It is this same principle of differences in solubility among phosphate phases that enables (bio)apatite to be added to lead-contaminated soil and cause the precipitation of the highly insoluble lead-phosphate mineral pyromorphite (e.g., Ma et al. 1993; Lower et al. 1998; Mavropoulos et al. 2002; Sneddon et al. 2006).

Our proposed mechanism for the fluoridation of the dentin and enamel in horse-tooth wafers begins with an initial process of selective dissolution of the most soluble crystallites, i.e., the most carbonate-rich, smallest, and atomically disordered bioapatite crystallites. We have spectroscopic evidence that this selective process occurs in the aqueous dissolution of bone in the absence of fluoride (Pasteris and Scully, unpublished data). The initial tooth dissolution releases calcium and phosphate, as well as carbonate, to the solution and enhances porosity and permeability within the sample. In the presence of fluoride in the solution, (nearly pure) fluorapatite reaches saturation, nucleates (either heterogeneously onto the bioapatite or homogeneously within the nanopores of the tooth), and precipitates very near the place from which the calcium was released. It is possible that an actual thin coating of FAp forms on the sample's surface, and that the thickness of each FAp grain is less than the depth of penetration of the laser, thereby causing spectra of both FAp and bioapatite to be recorded. We infer that this precipitation is kinetically controlled, which accounts for the recorded similarity in the solid's composition in the presence of widely different NaF concentrations after identical amounts of reaction time. Kinetic control of the process also could account for why the spectral progression is modeled well by the addition of (i.e., replacement by) essentially end-member fluorapatite. That the fluoridation process is controlled by the inherent solubility of the bioapatite is also supported by the much greater degree of fluoridation in dentin than in the adjacent, much less soluble enamel.

Concluding remarks

The proposed control of dentin- and enamel-fluoridation by solubility and kinetic factors has important geochemical, mineralogic, and paleontologic implications. Our model suggests, for instance, that even groundwaters with a low concentration of fluoride, over time, could cause the transformation of large proportions of bone and tooth material into fluorapatite. Bulk chemical analyses of such materials, however, would record only the over-all increase in fluoride concentration, not the compositions of individual grains. Fluoridation appears to be one of a suite of chemical reactions that could cause dissolved components in groundwater to become sequestered in low-solubility apatite-like phases. The enhanced solubility of (carbonated) bioapatite over typical geological (OH-F-Cl) apatite suggests that the former could be especially useful in phosphate-based remediation of unwanted aqueous ions, e.g., lead (Hettiarachchi and Pierzynski 2004; Lin et al. 2005; Giammar et al. 2008). Kinetically controlled formation of new apatite grains to some extent could preserve, i.e., re-capture, some of the isotopic and trace-element signatures embedded in the original bioapatite. On the other hand, REE and other dissolved ions that stabilize extremely low-solubility apatite-analogs could thereby overprint their signatures onto the bulk tooth material.

Clearly, the enamel is chemically much more resistant to geochemical overprinting than is the dentin, due in large part to enamel's larger grain size and lower carbonate concentration, which make it much less soluble than dentin. This realization is encouraging to paleontologists and isotope geochemists who analyze enamel for purposes of paleoenvironmental reconstruction (Kolodny et al. 1996; Koch 1998; Kohn et al. 1999; MacFadden 2000; Sharp et al. 2000; Ambrose and Krigbaum 2003; Zazzo et al. 2004; Kohn et al. 2005; Kohn and Law 2006; Zanazzi et al. 2007), but it also raises questions about the efficacy of some of the dental fluoridation practices of most residents in the United States (cf. Fagin 2008).

Acknowledgments

We thank Ray Whilite for providing the modern horse's molar, Mitchell Sternlieb and Claude Yoder for synthesizing the fluorapatite sample, and John Freeman for assistance with the fluoridation experiments. We also appreciate the help of Jennifer Pasteris and Shuyi Man with the preparation of some of the plots. Matthew Kohn and an anonymous reviewer provided very helpful comments on an earlier version of the paper. This paper is based upon work partially supported by the National Science Foundation under grant no. 0210247 and by the Center for Materials Innovation at Washington University in St. Louis, Missouri.

References cited

Ambrose, S.H. and Krigbaum, J. (2003) Bone chemistry and bioarchaeology. Journal of Anthropological Archaeology, 22, 193–199.

Awonusi, A., Morris, M.D., and Tecklenburg, M.M.J. (2007) Carbonate assignment and calibration in the Raman spectrum of apatite. Calcified Tissue International, 81, 46–52.

Baig, A.A., Fox, J.L., Young, R.A., Wang, Z., Hsu, J., Higuchi, W.I., Chhettry, A., Zhuang, H., and Otsuka, M. (1999) Relationships among carbonated apatite solubility, crystallite size, and microstrain parameters. Calcified Tissue International, 64, 437–449.

Barry, A.B., Zhuang, H., Baig, A.A., and Higuchi, W.I. (2003) Effect of fluoride pretreatment on the solubility of synthetic carbonated apatite. Calcified Tissue International, 72, 236–242.

Berna, F., Matthews, A., and Weiner, S. (2004) Solubilities of bone mineral from archaeological sites: The recrystallization window. Journal of Archaeological Science, 31, 867–882.

Bryant, J.D., Froelich, P.N., Showers, W.J., and Genna, B.J. (1996) A tale of two quarries: Biologic and taphonomic signatures in the oxygen isotope composition of tooth enamel phosphate from modern and Miocene equids. Palaios, 11, 397–408.

Carden, A. and Morris, M.D. (2000) Application of vibrational spectroscopy to the study of mineralized tissues (review). Journal of Biomedical Optics, 5, 259–268.

Cerling, T.E. and Sharp, Z.D. (1996) Stable carbon and oxygen isotope analysis of fossil tooth enamel using laser ablation. Palaeogeography, Palaeoclimatology, Palaeoecology, 126, 173–186.

Daculsi, G., Bouler, J.J., and LeGeros, R.Z. (1997) Adaptive crystal formation in normal and pathological calcifications in synthetic calcium phosphate and related biomaterials. International Review of Cytology, 172, 129–189.

Elliott, J.C. (2002) Calcium phosphate biominerals. In M.J. Kohn, J. Rakovan, and J.M. Hughes, Eds., Phosphates—Geochemical, Geobiological, and Materials Importance, 48, p. 427–453. Reviews in Mineralogy and Geochemistry, Mineralogical Society of America, Chantilly, Virginia.

Eppell, S.J., Tong, W., Katz, J.L., Kuhn, L., and Glimcher, M.J. (2001) Shape and size of isolated bone mineralites measured using atomic force microscopy. Journal of Orthopaedic Research, 19, 1027–1034.

Fabig, A. and Herrmann, B. (2002) Trace elements in buried human bones: Intra-population variability of Sr/Ca and Ba/Ca ratios—diet or diagenesis? Naturwissenschaften, 89, 115–119.

Fagin, D. (2008) Second thoughts about fluoride. Scientific American, 2008, 74–81.

Giammar, D.E., Xie, L., and Pasteris, J.D. (2008) Immobilization of lead with nanocrystalline carbonated apatite present in fish bone. Environmental Engineering Science, 25, 725–735.

Glimcher, M.J. (2006) Bone: Nature of the calcium phosphate crystals and cellular, structural, and physical chemical mechanisms in their formation. In N. Sahai and M.A.A. Schoonen, Eds., Medical Mineralogy and Geochemistry, 64, p.

223–282. Reviews in Mineralogy and Geochemistry, Mineralogical Society of America, Chantilly, Virginia.
Gross, K.A. and Berndt, C.C. (2002) Biomedical application of apatites. In M.J. Kohn, J. Rakovan, and J.M. Hughes, Eds., Phosphates—Geochemical, Geobiological and Material Importance, 48, p. 631–672. Reviews in Mineralogy and Geochemistry, Mineralogical Society of America, Chantilly, Virginia.
Harlov, D.E. and Förster, H.-J. (2003) Fluid-induced nucleation of (Y+REE)-phosphate minerals within apatite: Nature and experiment. Part II. Fluorapatite. American Mineralogist, 88, 1209–1229.
Hassan, A.A., Termine, J.D., and Haynes Jr., C.V. (1977) Mineralogical studies on bone apatite and their implications for radiocarbon dating. Radiocarbon, 19, 364–374.
Hettiarachchi, G.M. and Pierzynski, G.M. (2004) Soil lead bioavailability and in situ remediation of lead-contaminated soils: A review. Environmental Progress, 23, 78–93.
Hoppe, K.A., Amundson, R., Vavra, M., McClaran, M.P., and Anderson, D.L. (2004) Isotopic analysis of tooth enamel carbonate from modern North American feral horses: Implications for paleoenvironmental reconstructions. Palaeogeography, Palaeoclimatology, Palaeoecology, 203, 299–311.
Hughes, J.M. and Rakovan, J. (2002) The crystal structure of apatite, $Ca_5(PO_4)_3(F,OH,Cl)$. In M.J. Kohn, J. Rakovan, and J.M. Hughes, Eds., Phosphates—Geochemical, Geobiological, and Materials Importance, 48, p. 1–12. Reviews in Mineralogy and Geochemistry, Mineralogical Society of America, Chantilly, Virginia.
Koch, P.L. (1998) Isotopic reconstruction of past continental environments. Annual Review of Earth and Planetary Science, 26, 573–613.
Kohn, M.J. and Cerling, T.E. (2002) Stable isotope compositions of biological apatite. In M.J. Kohn, J. Rakovan, and J.M. Hughes, Eds., Phosphates—Geochemical, Geobiological, and Materials Importance, 48, p. 455–488. Reviews in Mineralogy and Geochemistry, Mineralogical Society of America, Chantilly, Virginia.
Kohn, M.J. and Law, J.M. (2006) Stable isotope chemistry of fossil bone as a new paleoclimate indicator. Geochimica et Cosmochimica Acta, 70, 931–946.
Kohn, M.J., Schoeninger, M.J., and Barker, W.W. (1999) Altered states: Effects of diagenesis on fossil tooth chemistry. Geochimica et Cosmochimica Acta, 63, 2737–2747.
Kohn, M.J., McKay, M.P., and Knight, J.L. (2005) Dining in the Pleistocene—Who's on the menu? Geology, 33, 649–652.
Kolodny, Y., Luz, B., Sander, M., and Clemens, W.A. (1996) Dinosaur bones: Fossils or pseudomorphs? The pitfalls of physiology reconstruction from apatite fossils. Palaeogeography, Palaeoclimatology, Palaeoecology, 126, 161–171.
LeGeros, R.Z. (1981) Apatites in biological systems. Progress in Crystal Growth and Characterization of Materials, 4, 1–45.
LeGeros, R.Z. and LeGeros, J.P. (1984) Phosphate minerals in human tissue. In J.O. Nriagu and P.B. Moore, Eds., Phosphate Minerals, p. 351–395. Springer-Verlag, New York.
LeGeros, R.Z., Glenn, F.B., Lee, D.D., and Glenn, W.D. (1985) Some physicochemical properties of deciduous enamel of children with and without pre-natal fluoride supplementation (PNF). Journal of Dental Research, 64, 465–469.
Lin, C.W., Lian, J., and Fang, H.H. (2005) Soil lead immobilization using phosphate rock. Water Air and Soil Pollution, 161, 113–123.
Lower, S.K., Maurice, P.A., and Traina, S.J. (1998) Simultaneous dissolution of hydroxylapatite and precipitation of hydroxypyromorphite: Direct evidence of homogeneous nucleation. Geochimica et Cosmochimica Acta, 62, 1773–1780.
Ma, Q.Y., Traina, S.J., and Logan, T.J. (1993) In situ lead immobilization by apatite. Environmental Science and Technology, 27, 1803–1810.
MacFadden, B.J. (2000) Middle Pleistocene climate change recorded in fossil mammal teeth from Tarija, Bolivia, and upper limit of the Ensenadan land-mammal age. Quaternary Research, 54, 121–131.
Mann, S. (2001) Biomineralization: Principles and concepts in bioinorganic materials. Oxford University Press, U.K.
Mavropoulos, E., Rossi, A.M., Costa, A.M., Perez, C.A., Moreira, J.C., and Saldanha, M. (2002) Studies on the mechanisms of lead immobilization by hydroxyapatite. Environmental Science and Technology, 36, 1625–1629.
McClellan, G.H. (1980) Mineralogy of carbonate fluorapatites. Journal of the Geological Society London, 137, 675–681.
Michel, V., Ildefonse, Ph., and Morin, G. (1996) Assessment of archaeological bone and dentine preservation from Lazaret Cave (Middle Pleistocene) in France. Palaeogeography, Palaeoclimatology, Palaeoecology, 126, 109–119.
Nammour, S., Rocca, J.P., Pireaux, J.J., Powell, G.L., Morciaux, Y., and Demortier, G. (2005) Increase of enamel fluoride retention by low fluence argon laser beam: A 6-month follow-up study in vivo. Lasers in Surgery and Medicine, 36, 220–224.
Nemliher, J.G., Baturin, G.N., Kallaste, T.E., and Murdmaa, I.O. (2004) Transformation of hydroxyapatite of bone phosphate from the ocean bottom during fossilization. Lithology and Mineral Resources, 39, 468–479.
Pan, Y. and Fleet, M.E. (2002) Compositions of the apatite-group minerals: Substitution mechanisms and controlling factors. In M.J. Kohn, J. Rakovan, and J.M. Hughes, Eds., Phosphates—Geochemical, Geobiological, and Materials Importance, 48, p. 13–49. Reviews in Mineralogy and Geochemistry, Mineralogical Society of America, Chantilly, Virginia.
Pasteris, J.D., Wopenka, B., Freeman, J.J., Rogers, K., Valsami-Jones, E., van der Houwen, J.A.M., and Silva, M.J. (2004) Lack of OH in nanocrystalline apatite as a function of degree of atomic order: Implications for bone and biomaterials. Biomaterials, 25, 229–238.
Pasteris, J.D., Yoder, C.H., Rogers, K.D., Sternlieb, M., and Man, S. (2007) Bone apatite: The secret is in the carbonate. Geological Society of America Abstracts with Programs, 39, 295–296.
Penel, G., Leroy, G., Rey, C., and Bres, E. (1998) MicroRaman spectral study of the PO_4 and CO_3 vibrational modes in synthetic and biological apatites. Calcified Tissue International, 63, 475–481.
Rakovan, J. (2002) Growth and surface properties of apatite. In M.J. Kohn, J. Rakovan, and J.M. Hughes, Eds., Phosphates—Geochemical, Geobiological, and Materials Importance, 48, p. 51–86. Reviews in Mineralogy and Geochemistry, Mineralogical Society of America, Chantilly, Virginia.
Sharp, Z.D., Atudorei, V., and Furrer, H. (2000) The effect of diagenesis on oxygen isotope ratios of biogenic phosphates. American Journal of Science, 300, 222–237.
Skinner, H.C.W. (2005) Mineralogy of bone. In O. Selinus, B. Alloway, J.A. Centeno, R.B. Finkelman, R. Fuge, U. Lindh, and P. Smedley, Eds., Essentials of Medical Geology, p. 667–693. Elsevier, New York.
Sneddon, I.R., Orueetxebarria, M., Hodson, M.E., Schofield, P.F., and Valsami-Jones, E. (2006) Use of bone meal amendments to immobilise Pb, Zn, and Cd in soil: A leaching column study. Environmental Pollution, 144, 816–825.
Streck, M.J. and Dilles, J.H. (1998) Sulfur evolution of oxidized arc magmas as recorded in apatite from a porphyry copper batholith. Geology, 26, 523–526.
Tacker, R.C. (2008) Carbonate in igneous and metamorphic fluorapatite: Two type A and two Type B substitutions. American Mineralogist, 93, 168–176.
Timlin, J.A., Carden, A., and Morris, M.D. (1999) Chemical microstructure of cortical bone probed by Raman transects. Applied Spectroscopy, 53, 1429–1435.
Trueman, C.N. and Tuross, N. (2002) Trace elements in recent and fossil bone apatite. In M.J. Kohn, J. Rakovan, and J.M. Hughes, Eds., Phosphates—Geochemical, Geobiological, and Materials Importance, 48, p. 489–521. Reviews in Mineralogy and Geochemistry, Chantilly, Virginia.
Wopenka, B. and Pasteris, J.D. (2005) A mineralogical perspective on the apatite in bone. Materials Science and Engineering C, 25, 131–143.
Zanazzi, A., Kohn, M.J., MacFadden, B.J., and Terry, D.O. (2007) Large temperature drop across the Eocene-Oligocene transition in central North America. Nature, 445, 639–642.
Zazzo, A., Lécuyer, C., and Mariotti, A. (2004) Experimentally-controlled carbon and oxygen isotope exchange between bioapatites and water under inorganic and microbioally-mediated conditions. Geochimica et Cosmochimica Acta, 68, 1–12.
Zocco, T.G. and Schwartz, H.L. (1994) Microstructural analysis of bone of the sauropod dinosaur *Seismosaurus* by transmission electron microscopy. Palaeontology, 37, 493–503.

Manuscript received January 7, 2008
Manuscript accepted July 10, 2008
Manuscript handled by Pupa Gilbert